

Mechano-chemical spinodal decomposition: A phenomenological theory of phase transformations in multi-component, crystalline solids

Shiva Rudraraju

Mechanical Engineering, University of Michigan

Anton Van der Ven

Materials, University of California Santa Barbara

Krishna Garikipati

Mechanical Engineering, Mathematics, University of Michigan

We present a new phenomenological treatment of phase transformations in multi-component crystalline solids driven by free energy density functions that are non-convex in mechanical and chemical variables. We identify the mechano-chemical spinodal as the region in strain-composition space where the free energy density function is non-convex. Our treatment describes diffusional phase transformations that are accompanied by symmetry breaking structural changes of the crystal unit cell due to mechanical instabilities in the mechano-chemical spinodal. This approach is relevant to phase transformations wherein the structural order parameters can be expressed as linear combinations of strains relative to a high-symmetry reference crystal. Because the local strains in an inhomogeneous, transforming microstructure can be finite, the elasticity problem must account for geometric nonlinearity. Furthermore, for physical consistency and mathematical well-posedness, we regularize the free energy density functions by interface free energy densities depending on gradients of the rapidly varying strain and composition fields. The resulting initial and boundary value problems are notoriously difficult to solve, chiefly due to the influence of nonlinear strain gradient elasticity. To overcome this last hurdle, we extend our recent work using spline basis functions to develop a robust numerical framework. It permits the solution of general initial and boundary value problems of mechano-chemical spinodal decomposition in three dimensions. The rich physics that ensues is explored in several numerical examples.

I. INTRODUCTION

Spinodal decomposition is a continuous phase transformation mechanism occurring throughout a solid that is far enough from equilibrium for its free energy density to lose convexity with respect to an internal degree of freedom. The latter could include the local composition as in classical spinodal decomposition described by Cahn and Hilliard¹, or a suitable non-conserved order parameter as in Allen and Cahn's theory for spinodal ordering². A key requirement for continuous transformations is that order parameters can be formulated to uniquely describe continuous paths connecting the various phases of the transformation. These phases then correspond to local minima on a single, continuous free energy density surface in that order parameter space. For classical spinodal decomposition inside a miscibility gap, all phases have the same crystal structure and symmetry, and the order parameter is simply the local composition. The existence of a single, continuous free energy density surface for all phases participating in a transformation implies, by geometric necessity, the presence of domains in order-parameter space where the free energy density is non-convex. Reaching those domains through supersaturation (by externally varying temperature or composition) makes the solid susceptible to a generalized spinodal decomposition.

Many important multi-component solids undergo phase transformations that couple diffusional redistribu-

tion of their components with a structural change of the crystallographic unit cell. One prominent example is the decomposition that occurs when cubic yttria-stabilized zirconia $\text{Zr}_{1-x}\text{Y}_x\text{O}_{2-x/2}$ is quenched into a two-phase equilibrium region between tetragonal $\text{Zr}_{1-x}\text{Y}_x\text{O}_{2-x/2}$ having low Y composition and cubic $\text{Zr}_{1-x}\text{Y}_x\text{O}_{2-x/2}$ having a high Y composition. Another occurs in Li battery electrodes made of spinel $\text{Li}_x\text{Mn}_2\text{O}_4$. Discharging to low voltages causes the compound to transform from cubic LiMn_2O_4 to tetragonal $\text{Li}_2\text{Mn}_2\text{O}_4$ through a two-phase diffusional phase transformation mechanism. As with simple diffusional phase transformations, these coupled diffusional/martensitic phase transformations can either occur through a nucleation and growth mechanism, or, if certain symmetry requirements are met, we will argue, through a *mechano-chemical spinodal decomposition mechanism* that we introduce here. We restrict ourselves to transformations between phases that satisfy a symmetry group-subgroup relationship, with the structural changes being weak as defined by Bhattacharya et al.³. This class of structural phase transformations generally proceeds without lattice invariant shears, allowing the reverse transformation to retrace its original path. If the structural distortions are small, the phase transformation can proceed coherently, at least during the initial stages of decomposition. We consider decomposition within single-crystalline solids. This is without loss of generality since polycrystals can be treated by allowing orientations of reference crystals to vary. Alternately a

single grain may be considered, with the effects of neighboring grains represented by grain boundary tractions⁴.

II. THE MECHANO-CHEMICAL SPINODAL IN TWO DIMENSIONS

For accessibility of the arguments, we first consider the two-dimensional analogue of the cubic to tetragonal transformation: the square to rectangle transformation. The high-symmetry square lattice will serve as the reference crystal relative to which strains are measured. Lower symmetry lattices that can be derived from the square lattice by homogeneous strain include the rectangle, the diamond and lattices where there are no constraints on the cell lengths and their angles.

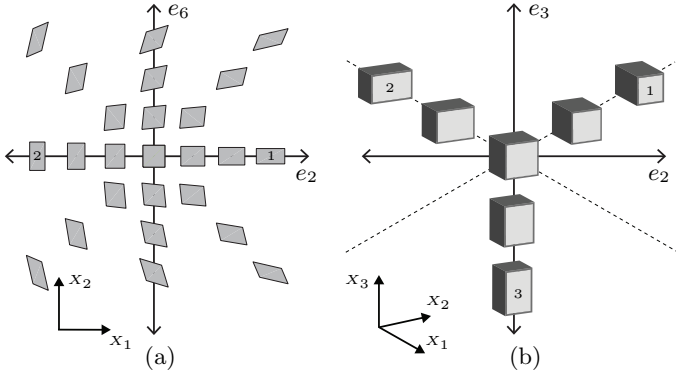


FIG. 1. (a) Square to rectangle transition (2D) in reparametrized strain space. (b) Cubic to tetragonal transition (3D) in reparametrized strain space (Equation[1]). Lattice vectors are labelled by the corresponding coordinate directions x_1, x_2, x_3 and the corresponding lower symmetry phases are labelled 1, 2, 3. The deformations shown in the sub-figures are area/volume preserving, respectively.

We use the composition c , varying between 0 and 1, as our order parameter for the chemistry of our binary two-dimensional solid. Symmetry breaking structural changes of the square lattice are naturally described by the strain relative to the high symmetry square lattice. The elastic free energy density is also a function of strain. In both contexts, strain will in general be of finite magnitude. Following Barsch & Krumhansl⁵, we use the Green-Lagrange strain tensor, \mathbf{E} , relative to the square lattice. Rotations are exactly neutralized in this strain measure; for any rigid body motion, $\mathbf{E} = \mathbf{0}$ (Supporting Information). In two dimensions, the relevant strain components are E_{11}, E_{22} and $E_{12} = E_{21}$. However, it is more convenient to use linear combinations of these components that transform according to the irreducible representations of the point group of the high symmetry square lattice. In two dimensions, these include $e_1 = (E_{11} + E_{22})/\sqrt{2}$, $e_2 = (E_{11} - E_{22})/\sqrt{2}$ and $e_6 = \sqrt{2}E_{12}$. Here, e_1 and e_6 reduce to the dilatation and shear strain, respectively in the infinitesimal strain limit. The strain measure e_2

uniquely maps the square lattice into the two rectangular variants [Figure 1a]: positive and negative e_2 generate the rectangles elongated along the global X_1 and X_2 directions, respectively. The equivalence of the rectangular variants under the point group symmetry of the square lattice ($e_2 = 0$) restricts the free energy density to even functions of e_2 .

If the crystalline solid has multiple chemical species, its free energy density dependence on e_1 , e_2 and e_6 can change with composition, c . Figure 2a illustrates a free energy density surface, $\mathcal{F}(c, e_2)$, for a binary solid that, at higher temperature, forms a solid solution having square symmetry. In this case \mathcal{F} is convex, a condition made precise by specifying positive eigenvalues of its Hessian matrix over the $\{c, e_2\}$ space. Additionally, $\mathcal{F}(c, 0)$ is a minimum with respect to e_2 for fixed c , making the square phase stable for all c at this temperature. However, at a lower temperature, \mathcal{F} may lose convexity, inducing the notion of a *mechano-chemical spinodal region*. We define it as the domain in $\{c, e_2\}$ space over which the Hessian matrix admits negative eigenvalues, as illustrated in Figure 2b. Here, we focus on the conditions $\partial^2 \mathcal{F} / \partial c^2 < 0$ and $\partial^2 \mathcal{F} / \partial e_2^2 < 0$. The square phase ($e_2 = 0$) remains stable at high composition ($c \sim 1$) with positive eigenvalues of the Hessian (Figure 2b). But it is mechanically unstable at low composition, with $\partial^2 \mathcal{F} / \partial e_2^2 < 0$ for $(c, e_2) \sim (0, 0)$, and has two symmetrically equivalent stable rectangular phases with $\partial^2 \mathcal{F} / \partial e_2^2 > 0$ at $(c, e_2) = (0, \pm s_e)$. While not shown in Figure 2b we assume that \mathcal{F} is convex with respect to e_1 and e_6 . Figure 2c illustrates a schematic temperature-composition phase diagram consistent with the free energy densities of Figure 2a-b. The square/cubic phase β , forms at high composition or at high temperature; the rectangle/tetragonal phase α , forms at low composition and low temperature. A large two-phase region separates them.

Consider our model binary solid, annealed at high temperature T_h , to form a solid solution in the square phase, β . Its state is at point A in Figure 2a, with $e_2 = 0$. It is then quenched into the two-phase region (Figure 2c) with free energy density at point B in Figure 2b. For a quench at sufficiently high rate, the dimensions of the square lattice, controlled by strains e_1 , e_2 and e_6 , and the composition remain momentarily unchanged. However, since the state at point B satisfies $\partial^2 \mathcal{F} / \partial e_2^2 < 0$ and $\partial^2 \mathcal{F} / \partial c^2 < 0$, there exist thermodynamic driving forces for segregation by strain and composition within the mechano-chemical spinodal.

Diffusion being substantially slower than elastic relaxation, the solid immediately deforms to either positive or negative e_2 , driven towards a local minimum at constant c . These deformations due to the mechanical instability will happen like many martensitic transformations where a mix of symmetrically equivalent rectangular variants coexist to minimize macroscopic strain energy. For finite but moderate strain, the transformation could proceed coherently, even if the two symmetrically equivalent

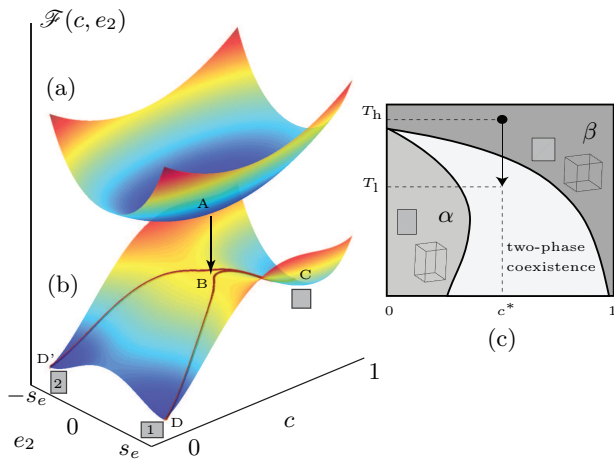


FIG. 2. (a) Free energy density for the 2D formulation at high temperature, and (b) at low temperature, showing the mechano-chemical spinodal along with two energy minimizing paths (brown lines) and their corresponding minimum energy strained structures. (c) Temperature-composition phase diagram.

rectangular variants coexist. We neglect non-essential complexities of this process and assume that, instantly upon quenching, finitely sized neighborhoods of the solid deform homogeneously into one of these rectangular variants at the original composition.

The solid also becomes susceptible to uphill diffusion because $\partial^2 \mathcal{F} / \partial c^2 < 0$ implies a negative diffusion coefficient. However, it does not occur at constant e_2 , since the valleys traversing the local minima, $\partial \mathcal{F} / \partial e_2 = 0$, between the square lattice at $c = 1$ and the rectangular lattices at $c = 0$ span intervals of negative and positive e_2 . Mechano-chemical spinodal decomposition sets in. Composition modulations are amplified: high c regions strive to be more square (point C) while low c regions strive to be more rectangular (points D or D'). However, since coherency is maintained, some neighborhoods in the solid will be frustrated from attaining strains that ensure minima, $\partial \mathcal{F} / \partial e_2 = 0$, for local values of c . Coherency strain-induced free energy penalties arise to alter the driving forces for purely chemical spinodal decomposition. Movie S5 in the supporting information shows the evolution of the state (c, e_2) of the material points on the free energy manifold \mathcal{F} .

III. MATHEMATICAL FORMULATION: THREE DIMENSIONS

Armed with the insight conveyed by the two-dimensional study, we next lay out the three-dimensional treatment, in which setting the considered phase transformations proceed via lattice deformation and diffusion. The arguments are made more concrete by considering the general mathematical form of the free energy density.

A. Strain order parameters

The strain measures e_1 - e_6 are first redefined using the full Green-Lagrange strain tensor components in three dimensions:

$$\begin{aligned} e_1 &= \frac{1}{\sqrt{3}}(E_{11} + E_{22} + E_{33}), & e_2 &= \frac{1}{\sqrt{2}}(E_{11} - E_{22}), \\ e_3 &= \frac{1}{\sqrt{6}}(E_{11} + E_{22} - 2E_{33}), & e_4 &= \sqrt{2}E_{23} = \sqrt{2}E_{32}, \\ e_5 &= \sqrt{2}E_{13} = \sqrt{2}E_{31}, & e_6 &= \sqrt{2}E_{12} = \sqrt{2}E_{21} \end{aligned} \quad (1)$$

In the limit of infinitesimal strains, e_1 describes the dilatation, while e_4 , e_5 and e_6 reduce to shears. The point group operations of the cubic crystal leave e_1 invariant since it is the trace of \mathbf{E} , while collecting each of the subsets $\{e_2, e_3\}$ and $\{e_4, e_5, e_6\}$ into a symmetry-invariant subspace whose elements transform into each other. The measures e_2 and e_3 are especially suited as order parameters to describe cubic to tetragonal distortions. All three tetragonal variants that emerge from the cubic reference crystal can be uniquely represented by these two measures. See Figure 1b where tetragonal distortions of the cubic crystal along the X_1 , X_2 and X_3 axes have been labelled as 1, 2 and 3, respectively. Deviations from the dashed lines in the e_2 - e_3 space of Figure 1b correspond to orthorhombic distortions of the cubic reference crystal. This role of e_2 and e_3 as structural order parameters to denote the degree of tetragonality, and to distinguish between the three tetragonal variants, complements their fundamental purpose as arguments of the elastic free energy density

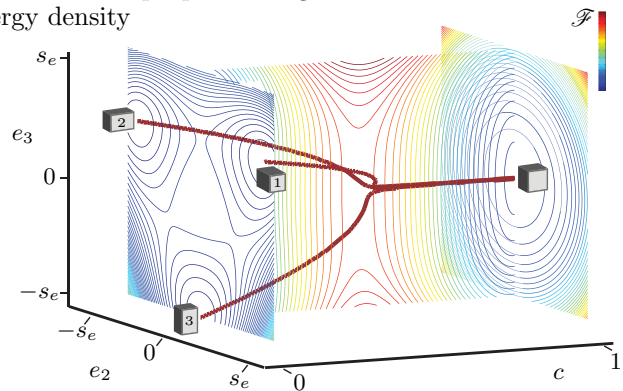


FIG. 3. Mechano-chemical spinodal for the 3D formulation depicted by contours of the free energy manifold along the e_2 - e_3 and e_3 - c planes. The three energy minimizing paths (brown lines) and their corresponding energy minimizing strained structures and are also shown.

B. The mechano-chemical spinodal in three dimensions

For brevity we write the strains as $\mathbf{e} = \{e_1, \dots, e_6\}$. We introduce further phenomenology by specifying that

$\mathcal{F}(c, \mathbf{e})$ is only one part of the total free energy density. It is a *homogeneous* contribution whose composition and strain dependence cannot be additively separated. Figure 3, for example, illustrates contour plots of $\mathcal{F}(c, \mathbf{e})$ on the e_2 - e_3 and e_3 - c planes for a binary solid having a temperature-composition phase diagram similar to that of Figure 2c. To generate the tetragonal α phase as illustrated in that diagram, the homogeneous free energy density as a function of strain must qualitatively follow the contours of the e_2 - e_3 plane at $c = 0$ in Figure 3. Here, the tetragonal variants are local minimizers of \mathcal{F} in e_2 - e_3 space, with equal minima. In turn, to obtain the cubic β phase, $\mathcal{F}(c, \mathbf{e})$ must follow the contours of the e_2 - e_3 plane at $c = 1$. Thus, \mathcal{F} changes smoothly from convex with respect to e_2 and e_3 on the $c = 1$ plane to non-convex at $c = 0$ to form the three variants of the tetragonal α phase. Importantly, the planes at $c = 0$ and $c = 1$ themselves must be minimum energy surfaces to represent the tetragonal α and cubic β phases, respectively. Movie S8 in the supporting information shows the evolution of the state (c, e_2, e_3) of the material points on the free energy manifold \mathcal{F} .

1. Gradient regularization of the free energy density

Following van der Waals⁸, and Cahn & Hilliard¹ in their treatment of non-uniform composition fields, we can extend the *total* free energy density beyond \mathcal{F} by writing it as a Taylor series, retaining terms that depend on the composition gradient, ∇c . We extend this gradient dependence to the strain measures $\nabla \mathbf{e}$, as did Barsch & Krumhansl⁵ following Toupin⁶. These gradient dependences appear in a non-uniform free energy density $\mathcal{G}(c, \mathbf{e}, \nabla c, \nabla \mathbf{e})$. Frame invariance of \mathcal{F} and \mathcal{G} is guaranteed since the members of \mathbf{e} are linear combinations of the tensor components of \mathbf{E} . They also must be invariant under point group operations of the cubic reference crystal.

C. Free energy functional

The crystal occupies a reference (undeformed) configuration Ω with boundary Γ . The total free energy, Π , is the integral of the free energy density $\mathcal{F} + \mathcal{G}$ over the solid with boundary contributions included. Thus, Π is a functional of the composition c and the displacement vector field \mathbf{u} , from which the strains are derived (see Supporting Information):

$$\Pi[c, \mathbf{u}] = \int_{\Omega} (\mathcal{F} + \mathcal{G}) dV - \sum_{i=1}^3 \int_{\Gamma_{T_i}} u_i T_i dS. \quad (2)$$

where traction vector component T_i is specified on the boundary subset $\Gamma_{T_i} \subset \Gamma$. Following the above authors

we include only quadratic terms in the gradients, but in a generalization we also allow cross terms between ∇c and $\nabla \mathbf{e}$ in the non-uniform contribution \mathcal{G} , which can therefore be written as

$$\begin{aligned} \mathcal{G}(c, \mathbf{e}, \nabla c, \nabla \mathbf{e}) = & \frac{1}{2} \nabla c \cdot \boldsymbol{\kappa}(c, \mathbf{e}) \nabla c \\ & + \sum_{\alpha, \beta} \frac{1}{2} \nabla e_{\alpha} \cdot \boldsymbol{\gamma}^{\alpha\beta}(c, \mathbf{e}) \nabla e_{\beta} \\ & + \sum_{\alpha} \nabla c \cdot \boldsymbol{\theta}^{\alpha}(c, \mathbf{e}) \nabla e_{\alpha}. \end{aligned} \quad (3)$$

Here $\boldsymbol{\kappa}$ is a tensor of composition gradient energy coefficients, each $\boldsymbol{\gamma}^{\alpha\beta}$ ($\alpha, \beta = 1, \dots, 6$) is a tensor of strain gradient energy coefficients, and each $\boldsymbol{\theta}^{\alpha}$ is a tensor of the mixed, composition-strain gradient energy coefficients. Note that, in general, these coefficients will be functions of the local composition and strain. The point group symmetry of the cubic reference crystal imposes constraints on the tensor components of $\boldsymbol{\kappa}$, $\boldsymbol{\gamma}^{\alpha\beta}$ and $\boldsymbol{\theta}^{\alpha}$ as well as on the form of \mathcal{F} .

While the gradient energies bestow greater accuracy upon the free energy description of solids with non-uniform composition and strain fields, they are essential at a more fundamental level if the homogeneous free energy density is non-convex. At compositions that render \mathcal{F} non-convex, the absence of a gradient energy term will allow spinodal decomposition characterized by composition fluctuations of arbitrary fineness, thus leading to non-unique microstructures—a fundamentally unphysical result⁷. With $\boldsymbol{\kappa} \neq \mathbf{0}$, the composition gradient energy penalizes the interfaces wherein composition varies rapidly between high and low limits. This ensures mathematical well-posedness and physically realistic results by way of unique microstructures. An essentially analogous situation exists with respect to the negative curvatures of \mathcal{F} in the e_2 - e_3 plane at low c , which drive the cubic lattice to distort into the tetragonal variants corresponding to the three free energy wells. Consider a solid with a homogeneous free energy density as in Figure 3 and a strain state lying between the valleys in the e_2 - e_3 plane at $c = 0$. Absent the strain gradient energy, mechanochemical spinodal decomposition would allow tetragonal variants of arbitrary fineness—an unphysical result, reflecting further mathematical ill-posedness. Retention of the strain gradient energy, ($\boldsymbol{\gamma}^{\alpha\beta} \neq \mathbf{0}$) penalizes interfaces of sharply varying strain between tetragonal variants to ensure mathematical well-posedness, unique microstructures and therefore, physically realistic results.

D. Governing equations of non-equilibrium chemistry

The free energy for non-homogeneous composition and strain fields, Eq. [2], must be a minimum at equilibrium. The state of a solid out of equilibrium will evolve to reduce the free energy $\Pi[c, \mathbf{u}]$. In formulating a kinetic

equation for the redistribution of atomic species through diffusion, we are guided by variational extremization of the free energy to identify the chemical potential, μ . Details of this calculation appear as supporting information. The result follows:

$$\begin{aligned} \mu = & \frac{\partial \mathcal{F}}{\partial c} - \nabla \cdot (\boldsymbol{\kappa}^s \nabla c) + \nabla c \cdot \frac{\partial \boldsymbol{\kappa}}{\partial c} \nabla c \\ & + \sum_{\alpha, \beta} \frac{1}{2} \nabla e_\alpha \cdot \frac{\partial \gamma^{\alpha\beta}}{\partial c} \nabla e_\beta \\ & + \sum_{\alpha} \left(\nabla c \cdot \frac{\partial \boldsymbol{\theta}^\alpha}{\partial c} \nabla e_\alpha - \nabla \cdot (\boldsymbol{\theta}^\alpha \nabla e_\alpha) \right), \quad (4) \end{aligned}$$

where $\boldsymbol{\kappa}^s = \frac{1}{2}(\boldsymbol{\kappa} + \boldsymbol{\kappa}^T)$ is symmetric. For solids where c tracks the composition of an interstitial element within a chemically inert host, such as Li in $\text{Li}_x\text{Mn}_2\text{O}_4$, μ in Eq. [4] corresponds to the chemical potential of the interstitial element. If c tracks the composition of a substitutional species, such as in alloys or on sublattices of complex compounds (e.g. the cation sublattice of yttria stabilized zirconia), μ is equal to the chemical potential difference between the substitutional species.

The common phenomenological relation for the flux is $\mathbf{J} = -\mathbf{L}(c, \mathbf{e}) \nabla \mu$, where \mathbf{L} is the Onsager transport tensor (see de Groot & Mazur⁹). For an interstitial species, \mathbf{L} is related to a mobility¹⁰, while it is a kinetic, intermixing coefficient for a binary substitutional solid¹¹. Inserting the flux in a mass conservation equation yields the strong form of the governing partial differential equation (PDE) for time-dependent mass transport. It is of fourth order in space due to the composition gradient dependence of μ in Equation [4]. See Supporting Information for strong and weak forms of this PDE.

E. Governing equations of mechanical equilibrium: Strain gradient elasticity

Mechanical equilibrium is assumed since elastic wave propagation typically is a much faster process than diffusional relaxation in crystalline solids. Equilibrium is imposed by extremizing the free energy functional with respect to the displacement field. Standard variational techniques lead to the weak and strong forms of strain gradient elasticity. The treatment is technical, for which reason we restrict ourselves to the constitutive relations that are counterparts to the chemical potential equation [4] for chemistry. Coordinate notation is used for transparency of the tensor algebra, and summation is implied over repeated spatial index, I . Details appear in Supporting Information. The final form of the equations is complementary to Toupin's⁶, since our derivation is relative to the reference crystal, Ω .

With the deformation gradient \mathbf{F} being related to the Green-Lagrange strain as $E_{KL} = \frac{1}{2}(F_{iK}F_{iL} - \delta_{KL})$, the first Piola-Kirchhoff stress tensor and the higher-order

stress tensor respectively, are given by

$$P_{iJ} = \sum_{\alpha} \frac{\partial(\mathcal{F} + \mathcal{G})}{\partial e_\alpha} \frac{\partial e_\alpha}{\partial F_{iJ}} + \sum_{\alpha} \frac{\partial \mathcal{G}}{\partial e_{\alpha,I}} \frac{\partial e_{\alpha,I}}{\partial F_{iJ}} \quad (5)$$

$$B_{iJK} = \sum_{\alpha} \frac{\partial \mathcal{G}}{\partial e_{\alpha,I}} \frac{\partial e_{\alpha,I}}{\partial F_{iJ,K}} \quad (6)$$

The higher-order stress \mathbf{B} , which is absent in classical, non-gradient elasticity¹² (and in earlier treatments of mechano-chemistry^{4,13}) makes the strong form of gradient elasticity a fourth order, nonlinear PDE in space (Supporting Information). The first three-dimensional solutions to general boundary value problems of Toupin's strain gradient elasticity theory at finite strains were recently presented by the authors¹⁴.

F. Numerical framework

The governing fourth-order PDEs of mass transport and gradient elasticity are solved numerically in weak form, wherein second-order spatial gradients appear on the trial solutions and their variations. Numerical solutions require basis functions that are continuous up to their first spatial gradients, at least. Our numerical framework (see Rudraraju et al.¹⁴) uses isogeometric analysis¹⁵ and the PetIGA code framework³¹ with spline basis functions, which can be constructed for arbitrary degree of continuity (Supporting Information). This framework has proven pivotal to the current work.

IV. NUMERICAL EXAMPLES

1. Two dimensional examples

We first consider a two-dimensional solid to better visualize the microstructures that can emerge from mechano-chemical spinodal decomposition. Plane strain elasticity is assumed, for which $E_{13}, E_{23}, E_{33} = 0$, giving $e_4, e_5 = 0$, and $e_3 = e_1/\sqrt{2}$, reducing Equations [1–6] to two dimensions. The discussion on two-dimensional mechano-chemical spinodal decomposition (Figure 2) holds: as a particular parameterization of $\mathcal{F}(c, e_1, e_2, e_6)$ we consider a regular solution model as a function of c at zero strain. At $c = 0$, $\mathcal{F}(c, e_1, e_2, e_6)$ is double-welled in e_2 corresponding to the two rectangular variants. The gradient energy is $\mathcal{G}(\nabla c, \nabla e_2)$ with $\boldsymbol{\kappa} \neq \mathbf{0}$ and $\gamma^{22} \neq 0$, all other gradient coefficients being zero. See Supporting Information for specific forms of $\mathcal{F}(c, e_1, e_2, e_6)$ and $\mathcal{G}(\nabla c, \nabla e_2)$.

Figure 4 shows the evolution of microstructure over a 0.01×0.01 domain whose reference (initial) state has the square crystal structure and $c = 1$. The displacement component $u_1 = 10^{-5}$ on the right boundary ($X_1 = 0.01$), with the remaining boundaries fixed ($\mathbf{u} = \mathbf{0}$). An outward flux is imposed on the top and bottom boundaries causing a decrease in composition, c , starting from

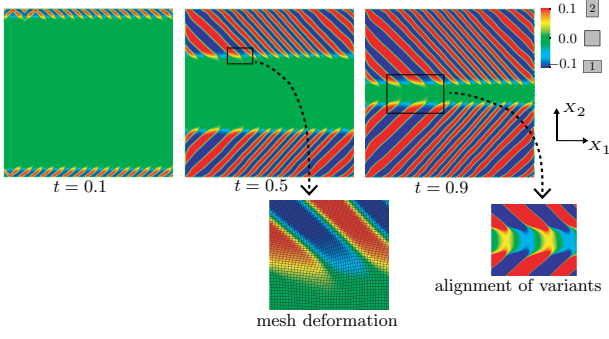


FIG. 4. Evolution of 2D microstructure during outflux from the top and bottom surfaces of a solid under plane strain. Contours show strain e_2 . Note the legend and corresponding square/rectangular variant crystal structures. The deformation and accompanying twinned microstructure are seen clearly in the distorted mesh.

the boundaries. As the composition falls, the homogeneous free energy density \mathcal{F} loses convexity and the state of the material (c, e_2) enters the mechano-chemical spinodal along $e_2 = 0$ (Figure 2b). The continuing outward flux first drives material near the top and bottom boundaries fully into the regime where the rectangular crystal structure is stable. As explained for Figure 2b, the negative curvature $\partial^2 \mathcal{F} / \partial e_2^2 < 0$ creates thermodynamic driving forces that distort the cubic structure, shown in green, into rectangular variants, which form as red/blue laminae (all e_2 values).

A laminar, twinned microstructure develops as the two rectangular variants form, distinguished by the sign of e_2 (see legend). The lamination accommodates the strain difference between the two rectangular variants to minimize the free energy. If strains were infinitesimal ($|e_1|, |e_2|, |e_6| \gtrsim 0$) e_2 would correspond to shear along directions that are rotated $\pi/4$ radians from the crystal axes. But finite strain is of interest here, as seen in the range $-0.1 \leq e_2 \leq 0.1$, and the deformations state is more complex. The twinning and coherency strains are seen in the distorted mesh of discretization (inset of top center panel). The undeformed mesh cells are squares, and hence the numerical discretization strikingly delineates the kinematics of the cubic to rectangular transformation, and highlights the rectangular twins as well as the concentrated distortions along the twin boundaries. Movie S6 in the supporting information shows such mesh distortion and formation of the rectangular twins with a different form of the function \mathcal{F} .

The long-range nature of elasticity forces like rectangular variants to align even when separated by an untransformed square phase. This is first seen in the finger-like extensions of strain contours from the rectangular variants into the square phase in Figure 4, followed by their alignment and eventual incorporation into laminae of the same variant (top right panel and its evolution shown as an inset).

The fineness of laminae depends on the

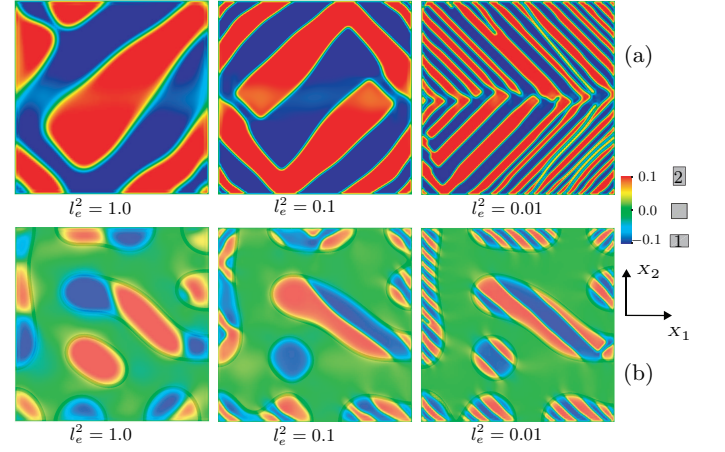


FIG. 5. Microstructure controlled by elastic gradient length scale parameter (l_e). Shown are the final contours of e_2 for the simulation of (a) outflux from top and bottom surfaces, and (b) quenching.

strain gradient elasticity length scale $l_e \sim \sqrt{\gamma^{22} / \sqrt{\sum_{\alpha, \beta=1,2,6} (\partial^2 \mathcal{F} / \partial e_\alpha \partial e_\beta)^2}}$, as explored in Figure 5. For Figure 5a, the initial and boundary conditions are the same as in the example of Figure 4. Decreasing l_e weakens the penalty on the strain gradient ∇e_2 across neighboring, unlike rectangular variants and allows more twin boundaries. Notably, self-similarity is not maintained between microstructures for different l_e , even for the same initial and boundary value problem. We understand this to be the influence of elastic strain accommodation: To minimize the total free energy when the strain gradient penalty changes, the physics optimizes twin boundaries via laminations of different sizes as well as different patterns. Importantly however, crystal symmetry admits non-vanishing strain gradient energy coefficients beyond $\gamma^{22} \neq 0$ used in these simulations (Supporting Information). Furthermore, the composition dependence of \mathcal{F} could be more complex than the simple regular solution model used here. Given the already strong effect of l_e alone, we conjecture that varying these forms will have a significant influence on the resulting coherent twin microstructure. The proper form, while guided by crystal symmetry arguments must ultimately be determined experimentally or by first-principles statistical mechanical methods.

The example in Figure 5b further explores the influence of l_e . In this suite of computations, the unstrained material with an initially square microstructure, convex free energy density and composition having random fluctuations about $c = 0.45$ was quenched to a low temperature and into the mechano-chemical spinodal. The local composition and strain evolve under the thermodynamic driving forces detailed in the context of Figure 2. We draw attention, once again, to the changing identity of rectangular variants, their shapes and sizes depending on l_e . Also note the progressively finer lamination of rectan-

gular domains with decreasing l_e . Such studies suggest how dynamic mechano-chemical spinodal decomposition can lead to an atlas of microstructures, which in turn will determine material properties. Movies S1-S4 in the supporting information show the evolution of some of these microstructures.

A. A three dimensional study

This final example displays the full three-dimensional complexity of microstructures resulting from the mechano-chemical spinodal. The free energy density function used for the three-dimensional study appears as supporting information.

Figure 6 shows the equilibrium microstructure that results in a solid that is initially in the cubic phase, $c = 1$, subject to an outflux on all surfaces. The domain is a unit cube with displacement components $u_2, u_3 = 0.01$ on the boundary $X_1 = 1$, with zero displacement, $\mathbf{u} = \mathbf{0}$, on the boundary $X_1 = 0$. The cubic to tetragonal transformation takes place as $c \rightarrow 0$. Under these conditions all three tetragonal variants form, with an intricately interleaved microstructure for strain accommodation. Note the finer microstructures and changing pattern for smaller l_e . The inset shows the surface straining around a corner, delineated by the distorted mesh lines. Observe the three, oriented, tetragonal variants formed by twinning deformation from the initial cubic structure. See Movie S7 in the supporting information for a detailed view of the three-dimensional structure of these individual tetragonal variants. To the best of our knowledge, such a computation explicitly developing twinned structures during a cubic to tetragonal transformation has not been previously presented. We conjecture that similar interleaved microstructures develop when Li is added to cubic LiMn_2O_4 to form tetragonal $\text{Li}_2\text{Mn}_2\text{O}_4$.

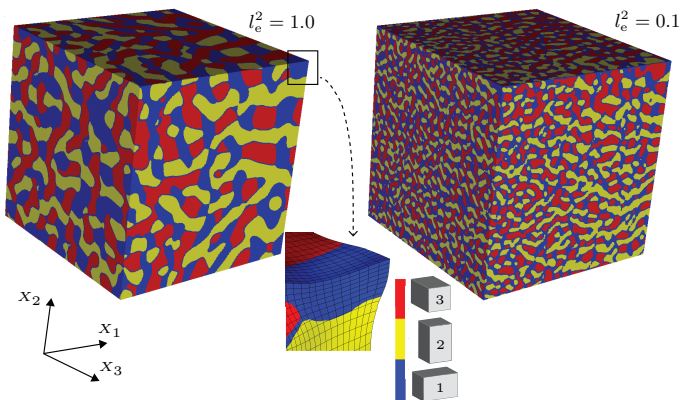


FIG. 6. Microstructure observed in 3D for different values of the elastic gradient length scale parameter (l_e). The three tetragonal variants appear in blue (variant 1), yellow (variant 2) and red (variant 3) for $c = 0$. The transformation strains are easily discerned in the distorted mesh.

V. DISCUSSION AND CONCLUSION

The phenomenology of mechano-chemical spinodal decomposition can be expected to occur inside multiphase coexistence regions between phases whose crystallographic unit cells are related by order parameters that are linear combinations of homogenous strains. The coexisting phases then all reside on a continuous free energy density surface expressed as a function of composition and strain. Crucial for the occurrence of mechano-chemical spinodal decomposition is a free energy density surface that changes from positive to negative curvature with respect to a strain order parameter upon varying composition. Diffusional fluxes, initiated either by a flux of species at the single crystal boundaries, or by uphill diffusion triggered due to negative curvature of the free energy with respect to composition, then have the potential to render an initially stable crystal structure mechanically unstable.

A change in mechanical stability with composition can be expected in solids forming high temperature phases that exhibit dynamical instabilities at low temperature with respect to phonon modes that break the symmetry of the crystal unit cell. An accumulating body of first-principles calculations of Born-Oppenheimer surfaces have shown that many high temperature phases are indeed mechanically unstable at low temperature^{16,17}. Phases that are mechanically unstable at low temperature can be stabilized at high temperature through large anharmonic vibrational excitations^{18–22}, usually becoming stable through a second order phase transition. For a subset of these chemistries, the free energy as a function of strain order parameters is convex and stable above the transition temperature, but becomes non-convex and mechanically unstable below the transition temperature²². If alloying a compound that undergoes such a second order structural transition tends to stabilize the high symmetry phase, it should produce a free energy surface as illustrated in both Figures 2b and Figure 3, and thereby make the solid susceptible to mechano-chemical spinodal decomposition.

We expect mechano-chemical spinodal decomposition to occur in a wide range of chemistries. One possible example, as described in the introduction, is the decomposition of cubic yttria stabilized zirconia^{24,25} upon quenching from the high temperature cubic phase into a two-phase region separating a low-Y tetragonal phase from a Y-rich cubic phase. While the precise mechanism and nature of the cubic to tetragonal transition of pure ZrO_2 remains to be resolved¹⁹, first-principles calculations predict that the cubic form of ZrO_2 is dynamically unstable with respect to transformation to the tetragonal variant²³. A rigorous statistical mechanical treatment is required to determine whether the cubic to tetragonal transition of pure ZrO_2 is accompanied by a change in the sign of the curvature of the free energy density with respect to e_2 and e_3 ²². If this proves to be the case, it too would be susceptible to mechano-chemical spinodal de-

composition upon quenching, consistent with the coherent spinodal microstructures between tetragonal and cubic phases observed in single crystal regions of quenched cubic $\text{Zr}_{1-x}\text{Y}_x\text{O}_{2-x/2}$ ²⁴.

A mechano-chemical spinodal also is likely to play a role in a variety of important electrode materials for Li-ion batteries, and intercalation compounds considered for two-dimensional nano-electronics. These include cubic LiMn_2O_4 transforming to tetragonal $\text{Li}_2\text{Mn}_2\text{O}_4$ ²⁷. While most mechano-chemical spinodal transitions will occur in three dimensions, many of the qualitative features of these transitions are more conveniently illustrated in two dimensions. Our two-dimensional studies should also prove relevant to understanding mechano-chemical phase transformations in two-dimensional layered materials for nano electronics. Materials such as TaS_2 , are susceptible to Peierls instabilities upon variation of the composition of adsorbed or intercalated guest species that donate to or extract electrons from the sheet-like host²⁸. Our phenomenological treatment by introduction of the concept of a mechano-chemical spinodal, coupled with gradient stabilization of the ensuing non-convex free energy in

strain-composition space, offers a framework with potential for extension to a wide range of phase transformation phenomena. Further, it also allows for a fully nonlinear (finite strain) gradient elasticity treatment of martensitic transformations, which have often been modeled with infinitesimal strains^{29,30}.

ACKNOWLEDGMENTS

The mathematical formulation for this work was carried out under an NSF CDI Type I grant: CHE1027729 “Meta-Codes for Computational Kinetics” and NSF DMR 1105672. The numerical formulation and computations have been carried out as part of research supported by the U.S. Department of Energy, Office of Basic Energy Sciences, Division of Materials Sciences and Engineering under Award #de-sc0008637 that funds the PRedictive Integrated Structural Materials Science (PRISMS) Center at University of Michigan.

-
- ¹ Cahn JW and Hilliard JE (1958) Free energy of a nonuniform system. I Interfacial energy *The Journal of Chemical Physics* 28:258–267
 - ² Allen SM and Cahn JW (1979) A microscopic theory for antiphase boundary motion and its application to antiphase boundary coarsening *Acta Metall.* 27:1085–1091
 - ³ Bhattacharya K, Conti S, Zanzotto G and Zimmer J (2004) Crystal symmetry and the reversibility of martensitic transformations *Nature* 428:55–59
 - ⁴ Voorhees PW and Johnson WC (2004) The thermodynamics of elastically stressed crystals *Solid State Physics: Advances in Research and Applications* 59:1–201
 - ⁵ Barsch GR and Krumhansl JA (1984) Twin boundaries in ferroelastic media without interface dislocations *Physical Review Letters* 53:1069–1072
 - ⁶ Toupin RA (1962) Elastic materials with couple-stresses *Archive for Rational Mechanics and Analysis* 11:385–414
 - ⁷ Hilliard JE (1970) Phase transformations *ASM 1970* 497–560
 - ⁸ van der Waals JD (1893) Thermodynamische theorie der capillariteit in onderstelling van continue dichtheidsverandering *Verhandelingen der Koninklijke Nederlandse Akademie* 1:3–56
 - ⁹ de Groot SR and Mazur P (1984) *Non-equilibrium thermodynamics*, Dover
 - ¹⁰ Van der Ven A, Bhattacharya J and Belak AA (2013) Understanding Li diffusion in Li-intercalation compounds *Accounts of Chemical Research* 46:1216–1225
 - ¹¹ Van der Ven A, Yu HC, Ceder G and Thornton K (2010) Vacancy mediated substitutional diffusion in binary crystalline solids *Progress in Materials Science* 55:61–105
 - ¹² Truesdell C and Noll W (1965) *The nonlinear field theories of mechanics*, Springer Verlag, Berlin Heidelberg
 - ¹³ Larche F and Cahn JW (1978) Non-Linear Theory of Thermochemical Equilibrium of Solids Under Stress *Acta Metallurgica* 26:53–60
 - ¹⁴ Rudraraju S, Van der Ven A and Garikipati K (2014) Three-dimensional isogeometric solutions to general boundary value problems of Toupin’s gradient elasticity theory at finite strains *Computer Methods in Applied Mechanics and Engineering* 278:705–728
 - ¹⁵ Cottrell J, Hughes TJR and Bazilevs Y (2009) *Isogeometric Analysis: Toward Integration of CAD and FEA*, Wiley, Chichester.
 - ¹⁶ Craievich PJ, Weinert M, Sanchez JM, Watson RE (1994) Local Stability of Nonequilibrium phases *Physical Review Letters* 72:3076–3079
 - ¹⁷ Grimvall G, Magyair-Koepe B, Ozolins V, Persson KA (2012) Lattice instabilities in metallic elements *Reviews of Modern Physics* 84:945–986
 - ¹⁸ Zhong W, Vanderbilt D, Rabe KM (1994) Phase Transitions in BaTiO_3 from First-Principles *Physical Review Letters* 73:1861–1864
 - ¹⁹ Fabris S, Paxton AT, Finnis MW (2001) Free energy and molecular dynamics calculations for the cubic-tetragonal phase transition in zirconia *Physical Review B* 63:094101
 - ²⁰ Bhattacharya J and Van der Ven A (2008) Mechanical Instabilities and Structural Phase Transitions: The Cubic to Tetragonal Transformation *Acta Materiala* 56:4226–4232
 - ²¹ Souvatzis P, Eriksson O, Katsnelson MI, Rudin SP (2008) Entropy driven stabilization of energetically unstable crystal structures explained from first principles theory *Physical Review Letters* 100:095901
 - ²² Thomas JC and Van der Ven A (2013) Finite-temperature properties of strongly anharmonic and mechanically unstable crystal phases from first principles *Physical Review B* 88:214111
 - ²³ Jomard G, Petit T, Pasturel A, Magaud L, Kresse G, Hafner J (1999) First-principles calculations to describe zirconia pseudopolymorphs *Physical Review B* 59:4044–

- 4052
- ²⁴ Krogstad JA, Kramer S, Lipkin DM, Johnson CA, Mitchell DRG, Cairney JM and Levi CG (2011) Phase Stability of t'-Zirconia-Based Thermal Barrier Coatings: Mechanistic Insights *Journal of the American Ceramic Society* 94:S168-S177
 - ²⁵ Chien FR, Uvic FJ, Prakash V and Heuer AH (1998) Stress-induced martensitic transformation and ferroelastic deformation adjacent microhardness indents in tetragonal zirconia single crystals *Acta Materialia* 46:2151–2171
 - ²⁶ Mamivand M, Zaeem MA, El-Kadiri H and Chen LQ (2013) Phase field modeling of the tetragonal-to-monoclinic phase transformation in zirconia *Acta Materialia* 61:5223–5235
 - ²⁷ Thackeray MM (1997) Manganese oxides for lithium batteries *Progress in Solid State Chemistry* 25:1-71
 - ²⁸ Rosnagel K (2010) Suppression and emergence of charge-density waves at the surfaces of layered 1T-TiSe₂ and 1T-TaS₂ by in situ Rb deposition *New Journal of Physics* 12:125018
 - ²⁹ Bouville M and Ahluwalia R (2007) Effect of lattice-mismatch-induced strains on coupled diffusive and displacive phase transformations *Physical Review B* 75(5):054110
 - ³⁰ Maraldi M, Wells G and Molari L (2011) Phase field model for coupled displacive and diffusive microstructural processes under thermal loading *Journal of the Mechanics and Physics of Solids* 59:1596–1612
 - ³¹ Collier N, Dalcín L and Calo VM (2013) PetIGA: High-Performance Isogeometric Analysis *arXiv* <http://arxiv.org/abs/1305.4452>

Supporting Information for Mechano-chemical spinodal decomposition: A phenomenological theory of phase transformation in multi-component crystalline solids

Shiva Rudraraju

Mechanical Engineering, University of Michigan

Anton Van der Ven

Materials, University of California Santa Barbara

Krishna Garikipati

Mechanical Engineering, Mathematics, University of Michigan

I. FINITE STRAIN KINEMATICS

In the interest of clarity and consistency with the main text, the Euclidean basis of our Cartesian coordinate system is denoted by \mathbf{X}_i , $i = 1, \dots, 3$, $\mathbf{X}_i \cdot \mathbf{X}_j = \delta_{ij}$. This constitutes a mild abuse of notation, because reference positions have also been denoted by X_1, X_2, X_3 . The high symmetry, cubic reference configuration of the crystal is denoted by Ω , on which material points are labelled by their position vectors $\mathbf{X} = X_1\mathbf{X}_1 + X_2\mathbf{X}_2 + X_3\mathbf{X}_3$. The deformation map from Ω to the current configuration of the crystal is $\boldsymbol{\varphi}(\mathbf{X}, t) = \mathbf{X} + \mathbf{u}$, where the displacement field \mathbf{u} was introduced in the main text. The deformation gradient tensor is $\mathbf{F} = \partial\boldsymbol{\varphi}/\partial\mathbf{X} = \mathbf{1} + \partial\mathbf{u}/\partial\mathbf{X}$. Using lower case indices to denote the components of vectors and tensors on the current configuration, and upper case indices for those on the reference configuration, we have the coordinate expression $F_{iJ} = \partial\varphi_i/\partial X_J = \delta_{iJ} + \partial u_i/\partial X_J$.

The Green-Lagrange strain tensor is $\mathbf{E} = \frac{1}{2}(\mathbf{F}^T\mathbf{F} - \mathbf{1})$, where $\mathbf{1}$ is the second-order isotropic tensor. We repeat this relation in coordinate notation from the main text: $E_{IJ} = \frac{1}{2}(F_{iI}F_{iJ} - \delta_{IJ})$. The polar decomposition theorem states that the deformation gradient can be decomposed multiplicatively as $\mathbf{F} = \mathbf{R}\mathbf{U}$, where \mathbf{R} is an (orthogonal) rotation tensor belonging to the space $\text{SO}(3)$. It therefore satisfies $\mathbf{R}^T\mathbf{R} = \mathbf{1}$. The other tensor in this decomposition, \mathbf{U} , is symmetric and positive-definite. From the polar decomposition it follows that \mathbf{E} as defined above is invariant to rotation of the current configuration. The requirement of material frame invariance dictates that the dependence of the free energy density on elasticity must be as a function of \mathbf{E} . Such a free energy density function is invariant to rotations on the current configuration.

II. THE CHEMICAL POTENTIAL: VARIATIONAL DERIVATION

Since the crystal is, in general, far from chemical equilibrium we follow the standard treatment of non-equilibrium thermodynamics to model the chemistry. In

order to obtain a relation for the chemical potential we consider variations on the composition field of the form $c_\varepsilon := c + \varepsilon\xi$, where ξ is a function such that, on the Dirichlet boundary, $\Gamma_c \subset \Gamma$, we have $c = \bar{c}$ and $\xi = 0$.

$$\frac{\delta}{\delta c}\Pi[c, \mathbf{u}] = \left. \frac{d\Pi[c + \varepsilon\xi, \mathbf{u}]}{d\varepsilon} \right|_{\varepsilon=0} \quad (1)$$

Carrying out the differentiation with respect to ε and integration by parts yields

$$\begin{aligned} \frac{\delta\Pi}{\delta c} = \int_{\Omega} \xi \left(\frac{\partial\mathcal{F}}{\partial c} - \nabla \cdot (\boldsymbol{\kappa}^s \nabla c) + \nabla c \cdot \frac{\partial\boldsymbol{\kappa}}{\partial c} \nabla c \right. \\ \left. + \sum_{\alpha, \beta} \frac{1}{2} \nabla e_\alpha \cdot \frac{\partial\gamma^{\alpha\beta}}{\partial c} \nabla e_\beta \right. \\ \left. + \sum_{\alpha} \left(\nabla c \cdot \frac{\partial\theta^\alpha}{\partial c} \nabla e_\alpha - \nabla \cdot (\theta^\alpha \nabla e_\alpha) \right) \right) dV \\ \left. + \int_{\Gamma} \xi \left(\boldsymbol{\kappa}^s \nabla c + \sum_{\alpha} \theta^\alpha \nabla e_\alpha \right) \cdot \mathbf{n} dS, \quad (2) \end{aligned}$$

where \mathbf{n} is the outward normal vector to Γ . At chemical equilibrium we have $\delta\Pi/\delta c = 0$, yielding two conditions:

$$\begin{aligned} \int_{\Omega} \xi \left[\frac{\partial\mathcal{F}}{\partial c} - \nabla \cdot (\boldsymbol{\kappa}^s \nabla c) + \nabla c \cdot \frac{\partial\boldsymbol{\kappa}}{\partial c} \nabla c \right. \\ \left. + \sum_{\alpha, \beta} \frac{1}{2} \nabla e_\alpha \cdot \frac{\partial\gamma^{\alpha\beta}}{\partial c} \nabla e_\beta \right. \\ \left. + \sum_{\alpha} \left(\nabla c \cdot \left(\frac{\partial\theta^\alpha}{\partial c} \nabla e_\alpha \right) - \nabla \cdot (\theta^\alpha \nabla e_\alpha) \right) \right] dV = 0 \quad (3) \end{aligned}$$

$$\int_{\Gamma} \xi \left[\boldsymbol{\kappa}^s \nabla c + \sum_{\alpha} \theta^\alpha \nabla e_\alpha \right] \cdot \mathbf{n} = 0 \quad (4)$$

Standard variational arguments lead to the conclusion that, for chemical equilibrium, the quantities within the

brackets must vanish on the corresponding domains Ω and Γ . The expression contained within brackets in the integrand of Equation [3] is the chemical potential μ . In the non-equilibrium setting that is of interest here, we continue to be guided by the above treatment and use the same definition for the chemical potential¹:

$$\begin{aligned} \mu = & \frac{\partial \mathcal{F}}{\partial c} - \nabla \cdot (\boldsymbol{\kappa}^s \nabla c) + \nabla c \cdot \frac{\partial \boldsymbol{\kappa}}{\partial c} \nabla c \\ & + \sum_{\alpha, \beta} \frac{1}{2} \nabla e_\alpha \cdot \frac{\partial \boldsymbol{\gamma}^{\alpha\beta}}{\partial c} \nabla e_\beta \\ & + \sum_{\alpha} \left(\nabla c \cdot \frac{\partial \boldsymbol{\theta}^\alpha}{\partial c} \nabla e_\alpha - \nabla \cdot (\boldsymbol{\theta}^\alpha \nabla e_\alpha) \right). \end{aligned} \quad (5)$$

Variants of Equation [4] appear in a proper variational derivation of chemical equilibrium—a detail that is sometimes overlooked in phase field treatments. We will impose chemical equilibrium of the boundary Γ , by requiring the term in brackets to vanish.

With the standard, phenomenological relation $\mathbf{J} = -\mathbf{L}(c, \mathbf{e}) \nabla \mu$ for the flux, the strong form of the governing PDE of mass balance follows:

$$\begin{aligned} \frac{\partial c}{\partial t} + \nabla \cdot \mathbf{J} &= 0 & \text{in } \Omega \\ -\mathbf{J} \cdot \mathbf{n} &= \bar{J} & \text{on } \Gamma \\ (\boldsymbol{\kappa}^s \nabla c + \sum_{\alpha} \boldsymbol{\theta}^\alpha \nabla e_\alpha) \cdot \mathbf{n} &= 0 & \text{on } \Gamma \\ c(\mathbf{X}) &= c_0(\mathbf{X}) & \text{at } t = 0 \end{aligned} \quad (6)$$

Note that we have assumed that there is no Dirichlet boundary; i.e. $\Gamma_c = \emptyset$, in stating the final strong form of this PDE. The conjugate boundary condition on the mass flux holds on the entire boundary Γ , in Equation [6₂]. Additionally, we have the boundary condition arising from requiring chemical equilibrium on Γ , in Equation [6₃]. Using standard variational arguments, the weak form of mass balance can be obtained by starting from [6]. Finally, we have the initial condition on composition, Equation [6₄]. The substitution of Equation [5] in $\mathbf{J} = -\mathbf{L} \nabla \mu$, followed by this phenomenological flux relation's substitution in (6₁) shows that this is a fourth order PDE in space.

A. On mass transport posed in the reference configuration

We note that the mathematical formulation of diffusion is commonly stated in the current (deformed) configuration, which is the true state of the solid. However, for crystalline solids (with negligible extended defects) it is more convenient to define Onsager transport coefficients and evaluate composition gradients on the reference (undeformed) configuration, here denoted by Ω . Diffusion in the crystalline solids results from atomic hops between well-defined crystal sites, which can always be mapped

onto a reference crystal structure. Increasingly, mobility coefficients in multi-component solids are calculated from first principles through the evaluation of Kubo-Green expressions in kinetic Monte Carlo simulations on the reference crystal in configuration Ω . Since the mobility tensor is reported on Ω , it is most convenient to adopt the Lagrangian description for diffusion over this configuration in single crystalline solids.

Our numerical implementation is based on the weak form, whose derivation we begin by first reintroducing ξ , now in the guise of a weighting function lying in the function space $\mathcal{Q} = \{\xi \in H^1(\Omega)\}$. We seek functions $c \in \mathcal{P} = \{c \in H^1(\Omega)\}$ such that

$$\begin{aligned} \int_{\Omega} \xi \frac{\partial c}{\partial t} dV + \int_{\Omega} \nabla \xi \cdot \mathbf{L} \nabla \left(\frac{\partial \mathcal{F}}{\partial c} + \frac{\partial \mathcal{G}}{\partial c} \right) dV \\ + \int_{\Omega} \nabla \cdot (\mathbf{L} \nabla \xi) \nabla \cdot (\boldsymbol{\kappa} \nabla c) dV \\ - \int_{\Gamma} \xi \bar{J} dS - \int_{\Gamma} (\mathbf{L} \nabla \xi) \cdot \mathbf{n} \nabla \cdot (\boldsymbol{\kappa} \nabla c) dS = 0 \end{aligned} \quad (7)$$

Equation [7] is obtained by multiplying ξ into [6₁], integrating by parts twice, and using the Neumann boundary condition [6₂]. Note that the higher-order Dirichlet boundary condition (6₃) has not been built into the function spaces as is commonly done in weak forms. Instead, it is imposed weakly using the method of Nitsche³⁻⁵ and extending the weak form to

$$\begin{aligned} \int_{\Omega} \xi \frac{\partial c}{\partial t} dV + \int_{\Omega} \nabla \xi \cdot \mathbf{L} \nabla \left(\frac{\partial \mathcal{F}}{\partial c} + \frac{\partial \mathcal{G}}{\partial c} \right) dV \\ + \int_{\Omega} \nabla \cdot (\mathbf{L} \nabla \xi) \nabla \cdot (\boldsymbol{\kappa} \nabla c) dV \\ - \int_{\Gamma} \xi \bar{J} dS - \int_{\Gamma} (\mathbf{L} \nabla \xi) \cdot \mathbf{n} \nabla \cdot (\boldsymbol{\kappa} \nabla c) dS \\ - \int_{\Gamma} \nabla \cdot (\boldsymbol{\kappa} \nabla \xi) (\mathbf{L} \nabla c) \cdot \mathbf{n} dS \\ + \int_{\Omega} \tau \nabla \xi \cdot \mathbf{n} \nabla c \cdot \mathbf{n} dS = 0 \end{aligned} \quad (8)$$

Equation [8] is based on the coupling tensor $\boldsymbol{\theta}^\alpha = \mathbf{0}$ for all α , and for $\boldsymbol{\kappa}, \boldsymbol{\gamma}^{\alpha\beta}$ independent of c , corresponding to the numerical examples presented in the main text. This weak form maintains consistency. Note that the second-to-last term that has been added over the form in Equation [7] is symmetric with the term preceding it. This formulation shows better numerical performance than the also-consistent formulation in which this additional term is preceded by a negative sign. Finally, τ is a stabilization parameter that is inversely proportional to the element size.

III. MECHANICAL EQUILIBRIUM

As explained in the main text, since elastic wave propagation is orders of magnitude faster than the kinetics of mass transport, it can be assumed that mechanical equilibrium is attained instantaneously for the prevailing composition field. To obtain the relevant equilibrium equations, we introduce variations on the displacement field: $\mathbf{u}_\varepsilon = \mathbf{u} + \varepsilon \mathbf{w}$, such that on the Dirichlet boundary Γ_{u_i} , the fields satisfy $u_i = \bar{u}_i$ and $w_i = 0$. We construct the first variation of $\Pi[c, \mathbf{u}]$ with respect to \mathbf{u} .

$$\frac{\delta}{\delta \mathbf{u}} \Pi[c, \mathbf{u}] = \frac{d}{d\varepsilon} \left(\int_{\Omega} (\mathcal{F}(c, \mathbf{e}_\varepsilon) + \mathcal{G}(c, \mathbf{e}_\varepsilon, \nabla c, \nabla \mathbf{e}_\varepsilon)) dV - \sum_{i=1}^3 \int_{\Gamma_{T_i}} u_{i\varepsilon} T_i dS \right) \Big|_{\varepsilon=0} \quad (9)$$

where \mathbf{e}_ε are obtained by first replacing \mathbf{u} by \mathbf{u}_ε in the kinematic relations for \mathbf{E} discussed above, which are then substituted in the relations for the reparameterized strains \mathbf{e} . We recall the constitutive relations for the first Piola-Kirchhoff stress and the higher-order stress, respectively:

$$P_{iJ} = \sum_{\alpha} \frac{\partial(\mathcal{F} + \mathcal{G})}{\partial e_{\alpha}} \frac{\partial e_{\alpha}}{\partial F_{iJ}} + \sum_{\alpha} \frac{\partial \mathcal{G}}{\partial e_{\alpha,I}} \frac{\partial e_{\alpha,I}}{\partial F_{iJ}} \quad (10)$$

$$B_{iJK} = \sum_{\alpha} \frac{\partial \mathcal{G}}{\partial e_{\alpha,I}} \frac{\partial e_{\alpha,I}}{\partial F_{iJK}} \quad (11)$$

Using these constitutive relations, Equation [9] can be manipulated to yield the Euler-Lagrange equation, which is also the weak form of mechanical equilibrium for a strain gradient elastic material, on Ω in terms of \mathbf{P} and \mathbf{B} . We retain coordinate notation in the interest of transparency:

$$\int_{\Omega} (P_{iJ} w_{i,J} + B_{iJK} w_{i,JK}) dV - \sum_{i=1}^3 \int_{\Gamma_{T_i}} w_i T_i dS = 0 \quad (12)$$

We introduce the normal and surface gradient operators, ∇^n and ∇^s , defined by

$$\nabla^n \psi = \nabla \psi \cdot \mathbf{n}, \text{ and } \nabla^s \psi = \nabla \psi - (\nabla^n \psi) \mathbf{n}. \quad (13)$$

Starting from Equation [12] and applying integration by parts several times we have the strong form of mechanical equilibrium for a strain gradient elastic material. See Rudraraju et al.² for detailed steps. The results of this variational treatment are analogous to those of Toupin⁶, except that it is carried out over the reference configura-

tion of the crystal, rather than its current configuration.

$$\begin{aligned} P_{iJ,J} - B_{iJK,JK} &= 0 \quad \text{in } \Omega \\ u_i &= \bar{u}_i \quad \text{on } \Gamma_{u_i} \\ P_{iJ} n_J - \nabla^n B_{iJK} n_K n_J - 2 \nabla_J^s (B_{iJK}) n_K \\ - B_{iJK} \nabla_J^s \nabla_K^s + (b_{LL} n_J n_K - b_{JK}) B_{iJK} &= T_i \quad \text{on } \Gamma_{T_i} \\ B_{iJK} n_J n_K &= 0 \quad \text{on } \Gamma \\ \llbracket n_J n_K B_{iJK} \rrbracket &= 0 \quad \text{on } \Upsilon_{L_i} \end{aligned} \quad (14)$$

Here, $\Gamma = \Gamma_{u_i} \cup \Gamma_{T_i}$ for $i = 1, 2, 3$, is the decomposition of the boundary surface into a subset with Dirichlet boundary condition on displacement component u_i and Neumann boundary condition on traction component T_i , respectively. Finally, Υ is a smooth boundary edge on which a jump in higher-order stress traction may arise. The fourth-order nature of the governing partial differential equation emerges on evaluating [10–11] and substituting in [14].

The Dirichlet boundary condition in [14₂] has the same form as for conventional elasticity. However, its dual Neumann boundary condition, [14₃] is notably more complex than its conventional counterpart, which would have only the first term on the left hand-side. Equation [14₄] is the higher-order Neumann boundary condition on the higher-order stress traction. The physical interpretation of this boundary condition in its homogeneous form is that the boundary has no mechanism to impose a moment on bonds at the atomic scale. Equation [14₅] specifies that there is no discontinuity of higher-order stress traction across edges. The weak form of mechanical equilibrium has already been encountered in [12]. For completeness we specify functional spaces: Find \mathbf{u} lying in $\mathcal{S} = \{\mathbf{u} \in H^2(\Omega_0) \mid u_i = \bar{u}_i \text{ on } \Gamma_{u_i}\}$ such that given functions T_i on Γ_{T_i} for $i = 1, 2, 3$ and tensors \mathbf{P} , \mathbf{B} defined by Equations [10–11], Equation [12] is satisfied for all \mathbf{w} lying in $\mathcal{V} = \{\mathbf{w} \in H^2(\Omega) \mid w_i = 0 \text{ on } \Gamma_{u_i}\}$.

IV. ISOGOMETRIC ANALYSIS FOR HIGH-ORDER PDES

Isogeometric Analysis (IGA) is a mesh-based numerical method with NURBS (Non-Uniform Rational B-Splines) basis functions. The NURBS basis functions have many desirable properties. They are partitions of unity with compact support, satisfy affine covariance and provide certain advantages over Lagrange polynomial basis functions, which are the mainstay of Galerkin finite element methods. These advantages include the imposition of higher-order, C^n -continuity, positivity, convex hull properties, and being variation diminishing. For a detailed discussion of the NURBS basis and IGA, interested readers are referred to Cottrell et al.⁷. However, we briefly present the construction of the basis functions.

The building blocks of the NURBS are univariate B-spline functions that are defined as follows: Consider pos-

itive integers p and n , and a non-decreasing sequence of values $\chi = [\xi_1, \xi_2, \dots, \xi_{n+p+1}]$, where p is the polynomial order, n is the number of basis functions, the ξ_i are coordinates in the parametric space referred to as knots (equivalent to nodes in FEM) and χ is the knot vector. The B-spline basis functions $B_{i,p}(\xi)$ are defined starting with the zeroth order basis functions

$$B_{i,0}(\xi) = \begin{cases} 1 & \text{if } \xi_i \leq \xi < \xi_{i+1}, \\ 0 & \text{otherwise} \end{cases} \quad (15)$$

and using the Cox-de Boor recursive formula for $p \geq 1$ ⁸

$$B_{i,p}(\xi) = \frac{\xi - \xi_i}{\xi_{i+p} - \xi_i} B_{i,p-1}(\xi) + \frac{\xi_{i+p+1} - \xi}{\xi_{i+p+1} - \xi_{i+1}} B_{i+1,p-1}(\xi) \quad (16)$$

The knot vector divides the parametric space into intervals referred to as knot spans (equivalent to elements in FEM). A B-spline basis function is C^∞ -continuous inside knot spans and C^{p-1} -continuous at the knots. If an interior knot value repeats, it is referred to as a multiple knot. At a knot of multiplicity k , the continuity is C^{p-k} . The boundary value problems in the main text consider only simple geometries, for which B-spline basis functions have sufficed. However, we outline the extension to NURBS basis functions for the sake of completeness, noting that the numerical formulation as presented is valid for any single-patch NURBS geometry. Using a quadratic B-spline basis (Figure S1), a C^1 -continuous one dimensional NURBS basis can be constructed.

$$N^i(\xi) = \frac{B_{i,2}(\xi)w_i}{\sum_{i=1}^{n_b} B_{i,2}(\xi)w_i} \quad (17)$$

where w_i are the weights associated with each of the B-spline functions. In higher-dimensions, NURBS basis functions are constructed as a tensor product of the one dimensional basis functions:

$$N^{ij}(\xi, \eta) = \frac{B_{i,2}(\xi)B_{j,2}(\eta)w_{ij}}{\sum_{i=1}^{n_{b1}} \sum_{j=1}^{n_{b2}} B_{i,2}(\xi)B_{j,2}(\eta)w_{ij}} \quad (2D) \quad (28)$$

$$N^{ijk}(\xi, \eta, \zeta) = \frac{B_{i,2}(\xi)B_{j,2}(\eta)B_{k,2}(\zeta)w_{ijk}}{\sum_{i=1}^{n_{b1}} \sum_{j=1}^{n_{b2}} \sum_{k=1}^{n_{b3}} B_{i,2}(\xi)B_{j,2}(\eta)B_{k,2}(\zeta)w_{ijk}} \quad (3D) \quad (29)$$

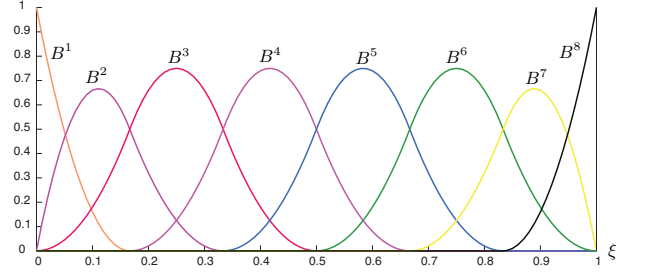


Figure S1: Quadratic ($p=2$) B-spline basis constructed from the knot vector $\chi = [0, 0, 0, 1/6, 1/3, 1/2, 2/3, 5/6, 1, 1, 1]$.

V. NUMERICAL EXAMPLES

The free energy density function for the two-dimensional examples is:

$$\begin{aligned} \mathcal{F}(c, e_1, e_2, e_6) = & 16d_c c^4 - 32d_c c^3 + 16d_c c^2 \\ & + \frac{2d_e}{s_e^2} (e_1^2 + e_6^2) \\ & + \frac{d_e}{s_e^4} c^4 + (2c - 1) \frac{2d_e}{s_e^2} e_2^2 \end{aligned} \quad (19)$$

$$\mathcal{G}(\nabla c, \nabla e_2) = \frac{1}{2} \nabla c \cdot \kappa \nabla c + \frac{1}{2} \nabla e_2 \cdot \lambda_e l_e^2 \nabla e_2 \quad (20)$$

where $d_c = 2.0$, $d_e = 0.1$, $s_e = 0.1$, $\kappa = 10^{-6}$ and $\lambda_e = 10^{-7}$. The problem domain is a square of dimensions 0.01×0.01 .

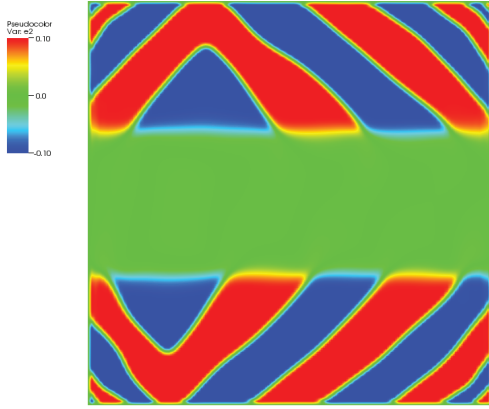
The free energy density function for the three-dimensional examples is:

$$\begin{aligned} \mathcal{F}(c, \mathbf{e}) = & 16d_c c^4 - 32d_c c^3 + 16d_c c^2 \\ & + \frac{3d_e}{2s_e^2} (e_1^2 + e_4^2 + e_5^2 + e_6^2) \\ & + \frac{3d_e}{2s_e^4} (e_2^2 + e_3^2)^2 \\ & + (1 - c) \frac{d_e}{s_e^3} e_3 (e_3^2 - 3e_2^2) \\ & + (2c - 1) \frac{3d_e}{2s_e^2} (e_2^2 + e_3^2) \end{aligned} \quad (21)$$

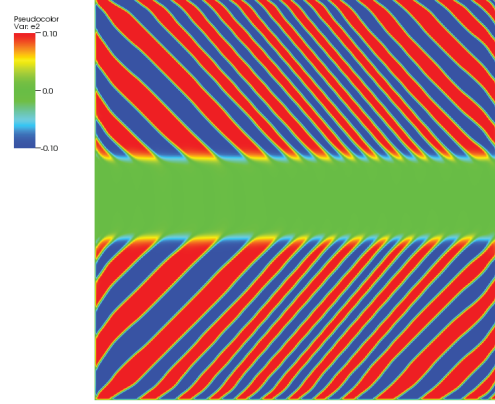
$$\begin{aligned} \mathcal{G}(c, \mathbf{e}, \nabla c, \nabla \mathbf{e}) = & \frac{1}{2} \nabla c \cdot \kappa \nabla c + \frac{1}{2} \nabla e_2 \cdot \lambda_e l_e^2 \nabla e_2 \\ & + \frac{1}{2} \nabla e_3 \cdot \lambda_e l_e^2 \nabla e_3 \end{aligned} \quad (22)$$

where $d_c = 2.0$, $d_e = 100.0$, $s_e = 0.1$, $\kappa = 10^{-2}$ and $\lambda_e = 1.0$. The problem domain is a unit cube. The strain gradient energy coefficient tensors have been chosen to be isotropic, $\gamma_{IJ}^{\alpha\beta} = \lambda_e l_e^2 \delta^{\alpha\beta} \delta_{IJ}$, and the three-dimensional formulation of the main text has been simplified here by setting the composition gradient-strain gradient coupling coefficients $\theta_{IJ}^\alpha = 0$.

VI. LIST OF VIDEOS



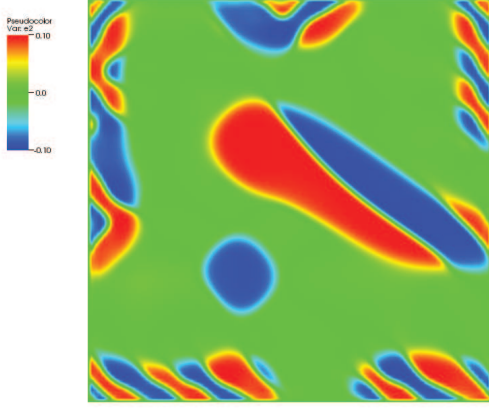
Movie S1[MovieS1.mp4]: Evolution of microstructure of the two-dimensional solid with outward flux corresponding to the plot for $l_e^2 = 0.1$ considered in Figure 5a of the main text.



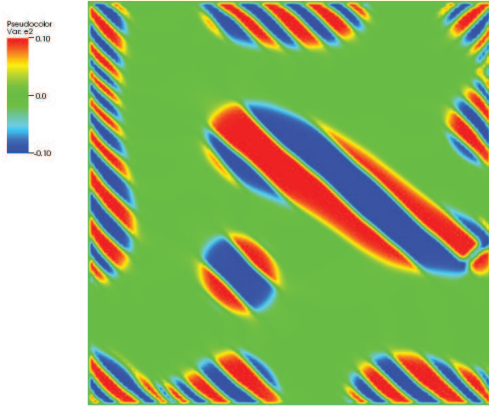
Movie S2[MovieS2.mp4]: Evolution of microstructure of the two-dimensional solid with outward flux corresponding to the plot for $l_e^2 = 0.01$ considered in Figure 5a of the main text.

-
- ¹ de Groot SR and Mazur P (1984) *Non-equilibrium thermodynamics*, Dover
- ² Rudraraju S, Van der Ven A and Garikipati K (2014) Three-dimensional isogeometric solutions to general boundary value problems of Toupin's gradient elasticity theory at finite strains *Computer Methods in Applied Mechanics and Engineering* 278:705–728
- ³ Nitsche JA (1971) Über ein variationsprinzip zur lösung Dirichlet-problemen bei verwendung von teilräumen, die keinen randbedingungen unterworfen sind *Abh. Math. Semin. Univ.* 36:9?15

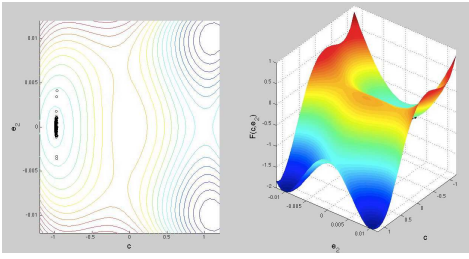
- ⁴ Arnold, DN, Brezzi, F, Cockburn, B, and Marini, DL (2001) Unified analysis of discontinuous galerkin methods for elliptic problems *SIAM J. Numer. Anal.* 39:1749?1779
- ⁵ Bazilevs, Y and Hughes, TJR (2007) Weak imposition of dirichlet boundary conditions in fluid mechanics *Comput. Fluids* 36:12?26
- ⁶ Toupin RA(1962) Elastic materials with couple-stresses *Archive for Rational Mechanics and Analysis* 11:385–414
- ⁷ Cottrell J, Hughes TJR and Bazilevs Y (2009) *Isogeometric Analysis: Toward Integration of CAD and FEA*, Wiley, Chichester.
- ⁸ Piegl L and Tiller W (1997) *The NURBS Book* Second ed., Springer-Verlag New York, Inc., New York.



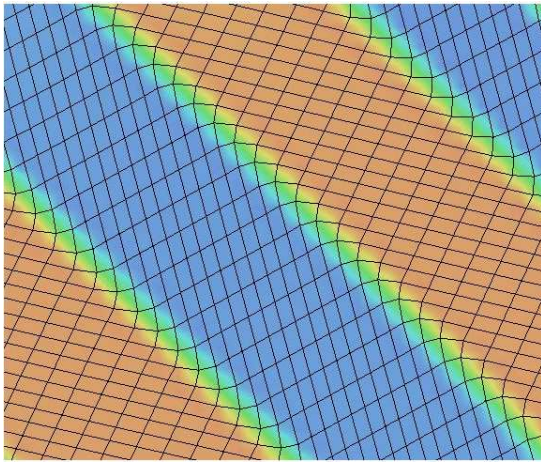
Movie S3[MovieS3.mp4]: Evolution of microstructure of the two-dimensional solid due to quenching from an initial composition of $c = 0.46$. This corresponds to the plot for $l_e^2 = 0.1$ considered in Figure 5b of the main text.



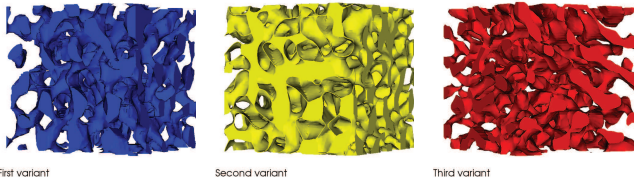
Movie S4[MovieS4.mp4]: Evolution of microstructure of the two-dimensional solid due to quenching from an initial composition of $c = 0.46$. This corresponds to the plot for $l_e^2 = 0.01$ considered in Figure 5b of the main text.



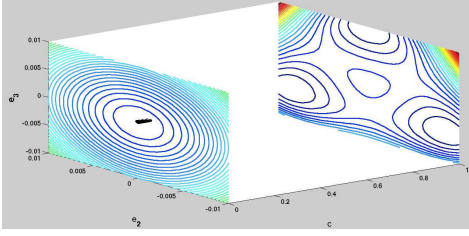
Movie S5[MovieS5.mp4]: Evolution of material points on the homogeneous free energy density surface, $\mathcal{F}(c, e_1, e_2, e_6)$ for the two-dimensional formulation, restricted to the $\{c, e_2\}$ sub-space. The microstructure that forms is similar to that in Movie S1.



Movie S6[MovieS6.mp4]: Zoomed-in view with distorted mesh lines showing the evolution of an initially square crystal lattice (green) into rectangular variants (red/blue) as the chemistry-driven cubic to rectangular transformation occurs, followed by the splitting of the variants into a twinned structure.



Movie S7 [MovieS7.mp4]: Isovolumes of the three interleaved tetragonal variants and the three-dimensional microstructure corresponding to the plot for $l_e^2 = 1.0$ considered in Figure 6 of the main text. For visual clarity, only a sub-domain of the simulation volume is shown.



Movie S8 [MovieS8.mp4]: Evolution of material points on the homogeneous free energy density surface, $\mathcal{F}(c, \mathbf{e})$ for the three-dimensional formulation, restricted to the $\{c, e_2, e_3\}$ sub-space. The microstructure that forms is similar to that in Movie S7.